Article

Hyperspectral imager with folded metasurface optics

MohammadSadegh Faraji-Dana, Ehsan Arbabi, Hyounghan Kwon, Seyedeh Mahsa Kamali, Amir Arbabi, John G. Bartholomew, and Andrei Faraon

ACS Photonics, **Just Accepted Manuscript** • DOI: 10.1021/acsphotonics.9b00744 • Publication Date (Web): 30 Jul 2019

Hyperspectral imager with folded metasurface optics

MohammadSadegh Faraji-Dana,[†,‡] Ehsan Arbabi,[†,‡] Hyounghan Kwon,[†,‡] Seyedeh Mahsa Kamali,[†,‡] Amir Arbabi,[¶] John G. Bartholomew,[†] and Andrei Faraon[*,†,‡]

†*T. J. Watson Laboratory of Applied Physics and Kavli Nanoscience Institute, California Institute of Technology, 1200 E. California Blvd., Pasadena, CA 91125, USA*

‡*Department of Electrical Engineering, California Institute of Technology, 1200 E. California Blvd., Pasadena, CA 91125, USA*

¶*Department of Electrical and Computer Engineering, University of Massachusetts Amherst, 151 Holdsworth Way, Amherst, MA 01003, USA*

E-mail: faraon@caltech.edu

Abstract

Hyperspectral imaging is a key characterization technique used in various areas of science and technology. Almost all implementations of hyperspectral imagers rely on bulky optics including spectral filters and moving or tunable elements. Here, we propose and demonstrate a line-scanning folded metasurface hyperspectral imager (HSI) that is fabricated in a single lithographic step on a 1-mm-thick glass substrate. The HSI is composed of four metasurfaces, three reflective and one transmissive, that are designed to collectively disperse and focus light of different wavelengths and incident angles on a focal plane parallel to the glass substrate. With a total volume of 8.5 mm^3, the HSI has spectral and angular resolutions of ~1.5 nm and 0.075°, over the 750 nm–850 nm and -15° to +15° degree ranges, respectively. Being compact, low-weight, and easy to fabricate and integrate with image sensors and electronics, the metasurface HSI opens up new opportunities for utilizing hyperspectral imaging where

strict volume and weight constraints exist. In addition, the demonstrated HSI exemplifies the utilization of metasurfaces as high-performance diffractive optical elements for implementation of advanced optical systems.

Keywords

Optical Metasurfaces, Diffractive optics, Nano-scale materials, Hyperspectral imaging

Introduction

Hyperspectral imaging, originally developed and utilized in remote sensing,[1,2] is a very powerful technique with applications in numerous areas of science and engineering such as archaeology,[3] chemistry, medical imaging,[4] biotechnology, biology,[5] bio-medicine, and production quality control.[6,7] In general, a hyperspectral imager (HSI) captures the spectral data for every point in an image. Therefore, the hyperspectral data for a 2D image is a 3D cube in which the first two dimensions are the spatial directions and the third one represents the spectrum (i.e., the imager records the function $I(x, y, \lambda)$).

Several methods and HSI platforms have been developed to acquire the 3D data cube using the existing 2D image sensors. One category of HSIs use tunable band-pass filters that can sweep through the desired spectral band.[8,9] In these devices, a 2D image is captured at each step in the scan, recording the optical power within the filter bandwidth. The required spectral scanning setups usually rely on a fine tuning mechanism that might not be fast or compact enough for many applications. A significant effort has been made to develop HSIs with faster and more compact spectral scanning schemes[10,11] and lower aberrations.[12] While acousto-optical and liquid crystal tunable filters provide solutions for fast spectral scanning, their low-throughput (under 50%) is still a disadvantage of these tunable filters .[9]

Another class of devices, snapshot HSIs, acquire the 3D data cube in a single shot without the need for a scanning mechanism.[13,14] However, they generally require heavy post-processing and

rely on some sort of sparsity in the spectral and/or spatial content of the image [15] as they are, in essence, compressive sensing methods. While their higher data rates and speeds make them suitable for recording transient scenes,[16] they generally suffer from low signal to noise ratios (SNR), and require significant computational resources.[15] Snapshot image mapping spectrometers (IMS), based on the idea of image slicing and dispersing each slice to obtain the spectral information and reconstruct the 3D data cube, work well only for low spatial resolution applications.[17] Additionally, the image mapper which is the primal part of IMS hyperspectral imaging systems needs to cut the scene with a high precision and often are not compact.[18]

A different group of HSIs are based on spatial scanning, and require a relative displacement of the HSI and the object of interest (i.e., either the object or the HSI is moved in space).[19] The spatial scanning is either done pixel by pixel (point scanning/whisk-broom) [20] or line by line (push-broom) using a slit in front of the HSI.[21] The whisk-broom technique requires 2D spatial scanning which results in longer acquisition times in comparison to the push-broom method. Thus, its applications are mostly limited to cases like confocal microscopy where measuring one point at a time while rejecting the signal from other points is of interest.[6] The push-broom HSIs[22] are faster and better-suited for applications such as air- and spaced-based hyperspectral scanning where the whole scene of interest might not be at hand at once.[23] One advantage of push-broom HSIs is that a large number of spectral-bands are captured without the burdensome post processing that is generally required for snapshot HSIs. Moreover, push-broom HSIs generally provide higher SNRs and better angular resolution compared to the snapshot ones.[21] Other approaches that indirectly obtain the 3D data cube, such as interferometric Fourier transform spectroscopic imaging,[24] in general rely on bulky and complicated optical setups, and are not well suited for compact and low-weight systems.[25]

A common challenge with almost all of the mentioned platforms is their compact, robust, and low-weight implementation, limited by the requirement for relatively complicated optical systems and reliance on mostly bulky conventional optical elements. In recent years, dielectric optical metasurfaces have overcome some of the limitations faced by the conventional optical elements .[26–29] Their ability to control the phase,[30–33] phase and polarization,[34] and phase and amplitude[35,36]

of light on a sub-wavelength scale and in compact form factors has made them very attractive for the implementation of compact optical systems.[37–39] In addition, the additional available degrees of freedom in their design allow for devices with enhanced control[40–42] that are otherwise not feasible.

Recently, a hyperspectral bio-detection technique using a set of dielectric metasurface resonators with different resonant wavelengths is shown.[43] The transmission spectra of the resonators is imaged using a tunable laser and an image sensor, and their resonance shifts induced by placing an analyte on the metasurface is computed and used for refractive index sensing. To obtain a hyperspectral image, illumination using a tunable laser is required, and the sample under study should be in physical contact with the metasurface.

Here, we propose and experimentally demonstrate a push-broom HSI based on the folded metasurface platform.[44] In this device, three reflective and one transmissive dielectric metasurfaces, which are monolithically fabricated on a glass substrate in a single lithographic step, disperse and focus light for various incident angles and wavelengths on a image plane parallel to the substrate. Working in the 750 nm–850 nm wavelength range, the metasurface HSI is polarization independent and provides more than 70 resolved spectral points in an 8.5 mm^3 volume. Spatially, the HSI has an angular resolution of ~0.075° and distinguishes about 400 angular directions in the ±15° range. The compact form factor, low weight, and high level of integrability of the metasurface HSIs make them very attractive for utilization into devices like consumer electronics, and more generally applications where there are stringent volume and weight limitations in addition to high performance requirements. Despite the prime advantages in size, weight, and throughput of the proposed metasurface HSIs, low scanning/capturing rates compared to snapshot HSIs might restrict some of their potentials for real-time applications. Nevertheless, these restricting factors can generally be resolved by using faster scanners and ultrafast high sensitivity cameras.

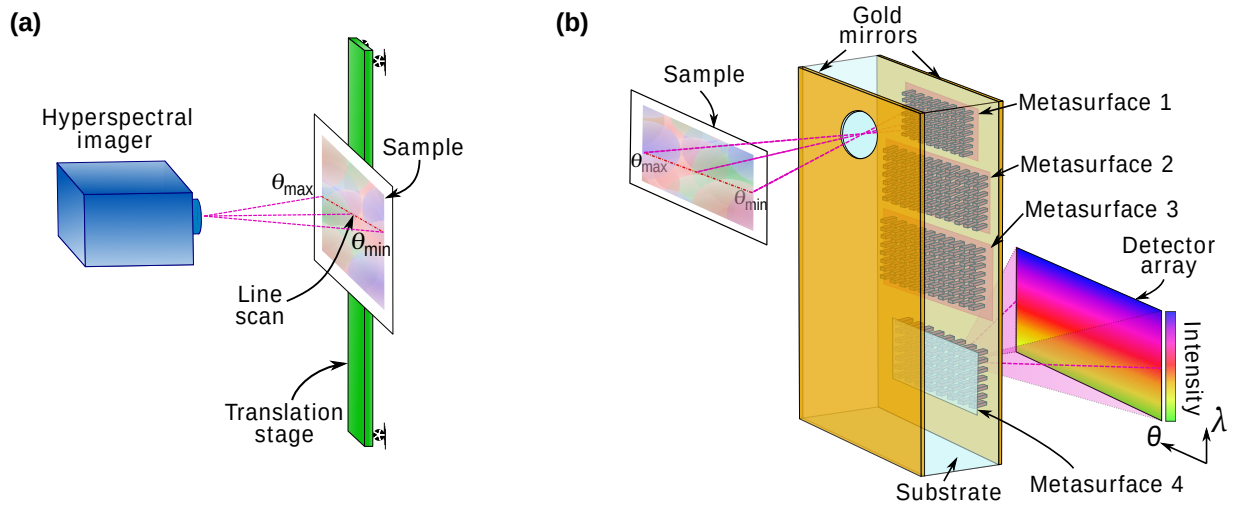

Figure 1: **Concept of a push-broom folded metasurface HSI.** (**a**) Schematic illustration of a push-broom hyperspectral imager. The spectral content is captured sequentially for different cross-sections of the object. (**b**) The proposed scheme for a folded metasurface hyperspectral imager. The device includes multiple reflective and transmissive metasurfaces each performing a different optical function. Light enters the device through an input aperture, interacts with the reflective metasurfaces while it is confined inside the substrate by the two gold mirrors, and exits the output aperture that has a transmissive metasurface built into it. Different wavelengths are dispersed in the vertical direction (λ), and various input angles are focused to different horizontal points.

Concept and design

A push-broom HSI is schematically shown in Fig. 1**a**. The HSI captures a 1D spatial image along the direction θ, measuring the spectrum at each pint along the line independently. The full 3D data cube can be formed by scanning the object in front of the HSI. Figure 1**b** schematically shows a folded metasurface push-broom HSI. The HSI includes one transmissive and three reflective metasurfaces patterned on one side of a 1-mm-thick fused silica substrate with gold mirrors on both sides. Light enters the HSI through an input aperture in one of the gold mirrors and is deflected into the substrate and vertically dispersed by the first metasurface (which acts as first-order blazed grating). The other two reflective metasurfaces together with the transmissive one focus light with different wavelengths and horizontal incident angles to diffraction-limited spots on the detector array plane that is parallel to the substrate. In this configuration, the transmissive metasurface, which is defined in the same lithography step as the reflective ones, simultaneously acts as the

output aperture.

Figure 2**a** illustrates ray tracing simulations of the designed HSI. The first metasurface acts as a blazed-grating with a 1-μm period, dispersing the collimated light coming from different angles, into angles centered at 33.46 degree (in the *y*-*z* plane) at the center wavelength of 800 nm. The phase profiles of the other three metasurfaces are optimized to provide near diffraction-limited focusing for the 750 nm–850 nm spectral and ±15 degree spatial range on a focal plane parallel to the substrate. For ease of measurements, the focal plane is designed to be 1 mm outside the substrate and parallel to it. The detailed design process of the three metasurfaces along with their phase profile coefficients are presented in Supplementary Section S1.

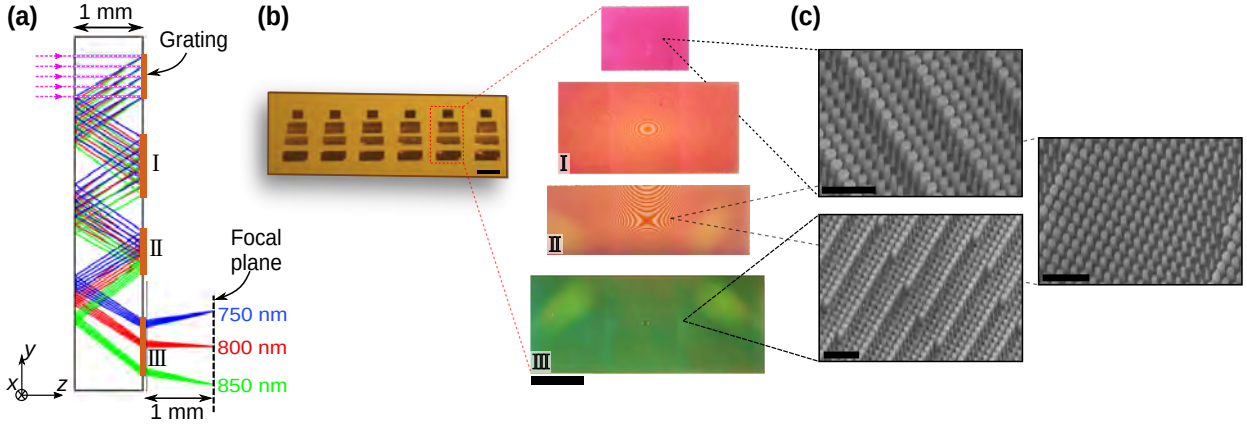

Figure 2: **Ray-optics design and pictures of the fabricated devices.** (**a**) Ray tracing simulation results of the folded metasurface HSI, shown for three wavelengths and a 0-degree incident angle. The system consists of 4 metasurfaces, first of which acts as a blazed grating dispersing different wavelengths. The following three metasurfaces (I, II, and III) are optimized to correct aberrations and focus the rays on the image plane for the desired wavelengths (750 nm–850 nm) and angels (-15 to +15 degrees). (**b**) An optical microscope image showing six HSIs on the same chip (left) and zoomed-in images of the metasurfaces that comprise one HSI (right). The images were captured before depositing the second gold layer. Scale bars: 1 mm (left) and 500 μm (right). (**c**) Scanning electron micrographs of parts of the fabricated metasurfaces. Scale bars: 1 μm.

The three reflective metasurfaces are implemented using a platform similar to the one used in.[44] The metasurfaces consist of α-Si nanoposts with rectangular cross-sections, resting on a 1-mm-thick fused silica substrate and capped by a 2-μm-thick SU-8 layer. The nanoposts' height and lattice constant are 395 nm and 246 nm, respectively, and a gold layer is deposited on the SU-8 layer to make the metasurfaces reflective. For the transmissive metasurface (III), the height and lattice

constant are 600 nm and 250 nm, respectively, and there is no gold mirror. The nanopost heights are in both cases chosen to achieve full 2π phase coverage, while minimizing the variation in the wavelength derivative of phase to keep the diffraction efficiency high over the whole bandwidth.[40] In addition, the lateral dimensions of the nanoposts are selected to make the metasurfaces polarization independent for an operation angle of 33.46 degrees.[44] We also confirmed that the metasurfaces are almost polarization independent for the entire operation bandwidth and angular range (see Supplementary Figs. S2 and S3 for simulated transmission and reflection phases). The blazed grating has a 1-μm period consisting of 4 nano-posts located on a lattice with a 250-nm lattice constant. The optimization procedure used for its design is similar to the approach taken in .[44] An initial structure was found using the high-NA high-efficiency design method,[45] and was then further optimized using the particle swarm optimization technique.

Experimental results

The metasurface HSI fabrication process was started with depositing a 600-nm-thick layer of α-Si on the fused silica substrate. Since the reflective and transmissive metasurfaces have different thicknesses (i.e., 395 nm and 600 nm, respectively), areas of the sample containing the reflective metasurfaces were first etched down to 395 nm. The patterns for both reflective and transmissive metasurfaces were then defined in a single electron beam lithography step, eliminating the need for additional alignment procedures. In addition, to avoid over-etching the thinner parts (corresponding to the reflective metasurfaces), dry etching was performed in two separate steps and the thinner parts were protected by a photoresist during the second step. After the etch and removal of the mask, the metasurfaces were covered by a 2-μm-thick SU-8 layer. The input and output apertures were then defined in ~100-nm-thick gold layers deposited on both sides of the substrate. The mirrors on both sides were then covered by another 2-μm-thick SU-8 layer for protection. Optical microscope images of the devices before deposition of the second (left) and first (right) gold mirrors are shown in Fig. 2**b**. Scanning electron micrographs of parts of the fabricated metasurfaces before capping

with the SU-8 layer are shown in Fig. 2**c**. See Supplementary Section S1 for fabrication details.

To characterize the fabricated HSI, the input aperture of the device was illuminated by a collimated beam from a tunable continuous-wave laser, and its focal plane was imaged using a custom-made microscope [Fig. 3**a**]. The setup was designed to allow for the input beam to be rotated in the horizontal plane around the input aperture (see Supplementary Fig. S4**a** and Section S1 for details of the measurement setup). The input wavelength was tuned in the 750 nm to 850 nm range in steps of 10-nm, and the input angle was changed in 5° separations. The intensity distribution in the focal plane was captured using the microscope. Figure 3**b** shows the captured intensities at 750, 800, and 850 nm for multiple incident angles. For comparison, the simulated expected focal spots positions are given in Fig. 3**c**, highlighting the spots where the zoomed-in distributions are plotted in Fig. 3**b**. Measured intensity distributions at other wavelengths and angles are given in Supplementary Fig. S5.

Figure 3**d** shows the simulated full width at half maximum (FWHM) along the *y* direction, the simulated spectral resolution, and the measured FWHMs at several points. Figure 3**e** shows similar results for the angular resolution of the device and the FWHM along the x direction. The good agreement observed between the simulated and measured FWHMs denotes the nearly diffraction-limited operation of the fabricated device. In addition, it can be seen from these results that the device has spectral and angular resolutions better than 1.4 nm and about 0.075 degree, respectively, across the whole bandwidth and for various angles. As a result, the demonstrated HSI can resolve more than 70 spectral and 400 angular points. The average variation in angular/spectral resolution is small (less than 10%) across the range of wavelengths and incident angles. Nonetheless, the spectral resolution is the highest at 0° because the spot size along the *y* direction is smallest at this angle due to a shorter focal length, and the improved angular resolution at 15° is due to increased spacing between spots along the *x* direction at larger incident angles. In addition, we measured the focal spots for multiple sets of wavelengths in the range with 1.5-nm separations, and several sets of angles with 0.1-degree distances. The results (see Supplementary Fig. S5) confirm the resolving power of the HSI.

The HSI focusing efficiency was measured using an approach similar to,[44] and its average value was found to be ~10% (see Supplementary Section S1 and Figs. S4**b** and S6 for the measurement details, setup, and measured efficiencies, respectively). The lower efficiency achieved here (in comparison to the spectrometer in[44]) is mostly because of using 4 metasurfaces instead of 3, especially as the transmissive metasurface has a large deflection angle of ~33 degrees in glass. The efficiency can be increased by using mirrors with higher reflectivities (like distributed Bragg reflectors), using anti-reflection coatings on the input and output apertures, and further optimizing the design and fabrication of the metasurfaces, especially the dispersive grating and the transmissive metasurface. The focusing efficiency reduces by ~ 36% at the incident angles of ±15 degrees. The reduction in efficiency at higher incident angles compared to the normal one can be attributed to different factors. Primarily, the effective aperture seen by oblique beams is smaller at higher incident angles. Furthermore, the diffraction grating, which is optimized at normal incidence, does not operate as efficiently at other incident angles. Finally, the phase profiles of the metasurfaces, slightly deviate from their optimal profiles at oblique incident angles.

To demonstrate the capability of the folded metasurface HSI in recovering 3D hyperspectral data cubes we used it to image an object with spatially varying spectral information. To this end, we designed and fabricated an imaging target with narrow transmission dips over the 750 nm–850 nm wavelength range (see Supplementary Section S2 and Fig. S8 for more information on the design and fabrication of the target). As shown in Fig. 4**a**, a broadband source (covering 750 nm–850 nm) was used to illuminate the object. The imaging optics in Fig. 4**a** mapped different points along a horizontal line on the target to different incident angles on the HSI input aperture within its acceptance range (see Supplementary Fig. S4**c** for details of the measurement setup). To measure the hyperspectral content, the target was vertically moved and the focal plane of the HSI was imaged at each step of the movement. This results in a 3D data cube, with a 2D image corresponding to each horizontal line on the target (see Supplementary Fig. S7 for details). Using the data in Fig. 3**c**, the intensity maps can be converted to angular/spectral data for each line. The inset in Fig. 4**a** shows the expected transmission dip wavelengths over the target. Figure 4**b** shows the captured

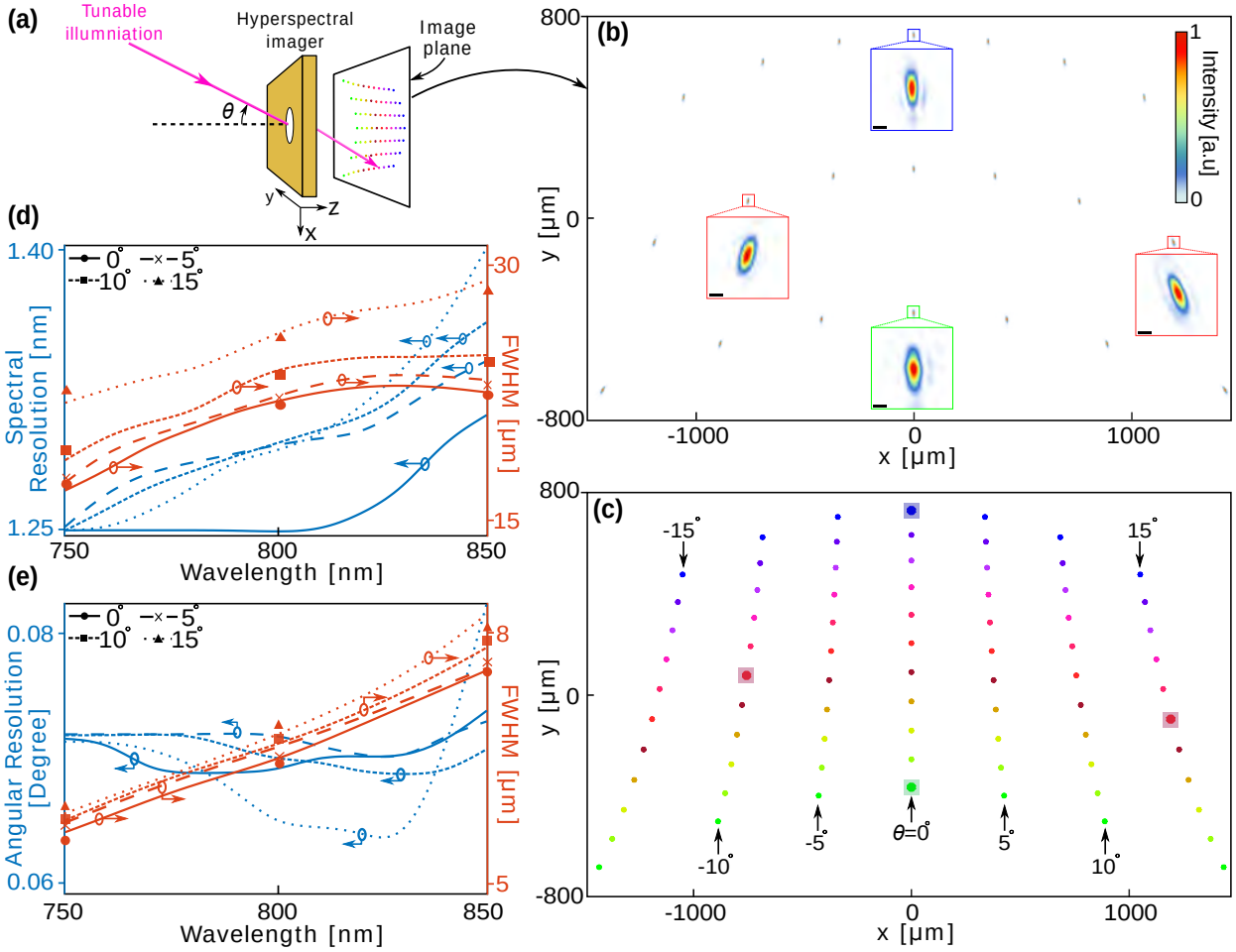

Figure 3: **Simulated and experimental characterization results of the folded metasurface HSI.** (**a**) Simplified schematic of the measurement setup. A collimated beam from a tunable laser illuminates the input aperture at various incidence angles, and the intensity distributions at the focal plane are captured. (**b**) Measured focuses on the image plane, shown for 3 wavelengths (750, 800, and 850 nm) and angles ranging from -15° to +15° with 5° increments. The insets show the zoomed-in version of intensity profiles (scale bars: 10 μm). (**c**) Simulated locations of the spots on the focal plane for wavelengths increasing from 750 nm (blue) to 850 nm (green) at 10-nm steps, and angles from -15° (left) to +15° (right) at 5° separations. The highlighted focal spots are magnified in the insets of **b**. (**d**) Simulated spectral resolution and vertical FWHM versus wavelengths, calculated at multiple incident angles. The measured FWHM values for three wavelengths are overlaid on the graph. (**e**) Simulated angular resolution and FWHM versus wavelengths calculated for multiple incident angles. Measured horizontal FWHM values at three wavelengths are overlaid on the graph.

images of the target at four different wavelengths in the range. For comparison, we also imaged the target using a tunable laser (TL) by scanning the illumination wavelength through the range (see Supplementary Fig. S4**d** for the measurement setup and other details). The data obtained with the TL setup is shown next to the HSI images in Fig. 4**b**, denoting a good agreement between the results. In addition, Fig. 4**c** shows the captured spectra along a vertical and a horizontal cut in the target, using both the HSI and the TL setup. We mostly attribute the minor differences between the two sets of measurements to the speckle noise observed in the images obtained using the tunable laser. The speckle noise was caused by the residual degrees of spatial and temporal coherence of the tunable laser which persisted despite the use of a rotating diffuser.

Conclusion

We demonstrated a push-broom metasurface hyperspectral imager with a volume of 8.5 mm^3 and weighing less than 20 mg, resolving more than 70 spectral and 400 angular points in the 750 nm–850 nm and ±15 degrees range, respectively. The significant reduction in size and weight of the device, achieved through the folded architecture design, makes the device a promising candidate for applications where compactness, low-weight, and robustness are of primary importance. In addition, many similar or different devices may be mass-produced in a single lithographic step, enabling multiple HSIs on the same chip, consequently covering a broader spectral range. For operation in the visible range, silicon nitride or titanium dioxide nano-post may be used instead of amorphous silicon ones. More broadly, as one of the first demonstrations of a meta-system consisting of multiple reflective and transmissive metasurfaces performing a complicated optical function in a small form factor, this work paves the way towards better realization of potentials of metasurfaces in implementing advanced functional optical and optoelectronic systems for operation under strict constraints.

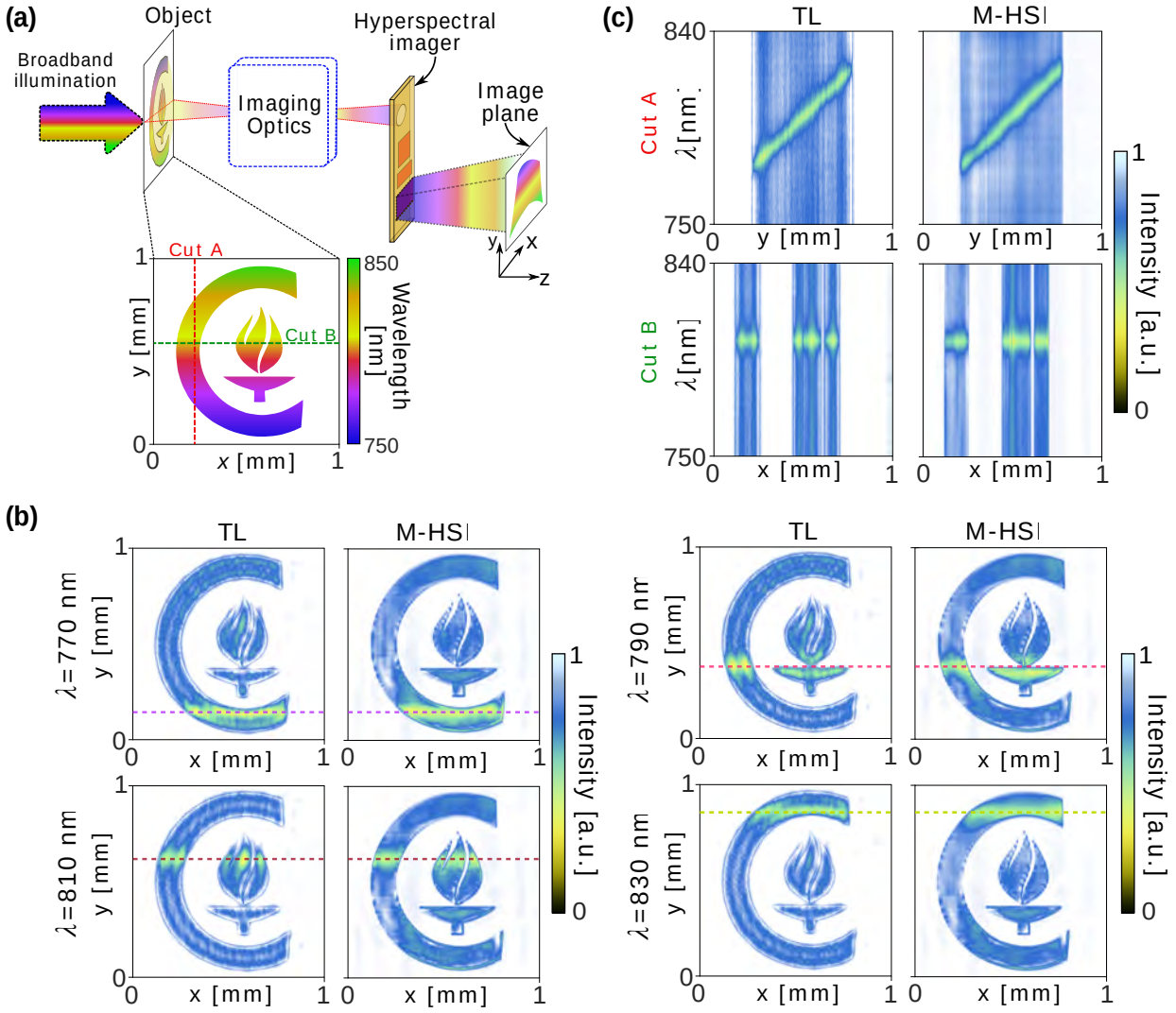

Figure 4: **Hyperspectral imaging of a target with the folded metasurface HSI (M-HSI) and a tunable laser.** (**a**) Simplified schematic of hyperspectral imaging a target with the HSI. The imaging optics maps different points along a horizontal line on the target to collimated beams with different incident angles on the HSI aperture. The image containing the spectral and angular data for the line is formed by the HSI in its focal plane and captured by a custom-built microscope. The inset shows the fabricated target, which has transmission dips with increasing center wavelength from bottom to the top. (**b**) Measured transmitted intensity of the object at four wavelengths captured by the metasurface HSI, compared with the ones measured using a tunable laser (TL). (**c**) Transmitted intensity profile of the object along the two cuts A and B, compared with the same results obtained using the tunable laser.

Acknowledgement

This work was supported by Samsung Electronics. M.F. was partly supported by the Natural Sciences and Engineering Research Council of Canada (NSERC). The device nano-fabrication was performed at the Kavli Nanoscience Institute at Caltech. Authors thank Dr. Jonathan Kindem for his help in measurements using the tunable laser.

Contribution

M.F., E.A., A.A. and A.F. conceived the experiment. M.F., E.A., and H.K. fabricated the samples. M.F, E.A., S.M.K., H.K. and J.G.B. performed the simulations, measurements, and analyzed the data. M.F., E.A., A.A. and A.F. co-wrote the manuscript. All authors discussed the results and commented on the manuscript.

Supporting Information Available

See Supplementary materials for supporting content.

References

(1) Goetz, A. F.; Vane, G.; Solomon, J. E.; Rock, B. N. Imaging spectrometry for earth remote sensing. *Science* **1985**, *228*, 1147–1153.

(2) Eismann, M. T. Hyperspectral remote sensing. 2012.

(3) Liang, H. Advances in multispectral and hyperspectral imaging for archaeology and art conservation. *Applied Physics A* **2012**, *106*, 309–323.

(4) Lu, G.; Fei, B. Medical hyperspectral imaging: a review. *Journal of biomedical optics* **2014**, *19*, 010901.

(5) Wang, Y.; Bish, S.; Tunnell, J. W.; Zhang, X. MEMS scanner enabled real-time depth sensitive hyperspectral imaging of biological tissue. *Optics Express* **2010**, *18*, 24101–24108.

(6) Boldrini, B.; Kessler, W.; Rebner, K.; Kessler, R. W. Hyperspectral imaging: a review of best practice, performance and pitfalls for in-line and on-line applications. *Journal of near infrared spectroscopy* **2012**, *20*, 483–508.

(7) Gowen, A.; O'Donnell, C.; Cullen, P.; Downey, G.; Frias, J. Hyperspectral imaging–an emerging process analytical tool for food quality and safety control. *Trends in food science & technology* **2007**, *18*, 590–598.

(8) Morris, H. R.; Hoyt, C. C.; Treado, P. J. Imaging spectrometers for fluorescence and Raman microscopy: acousto-optic and liquid crystal tunable filters. *Applied spectroscopy* **1994**, *48*, 857–866.

(9) Gat, N. Imaging spectroscopy using tunable filters: a review. Wavelet Applications VII. 2000; pp 50–65.

(10) Tack, N.; Lambrechts, A.; Soussan, P.; Haspeslagh, L. A compact, high-speed, and low-cost hyperspectral imager. Silicon Photonics VII. 2012; p 82660Q.

(11) Gupta, N.; Voloshinov, V. Hyperspectral imager, from ultraviolet to visible, with a KDP acousto-optic tunable filter. *Applied optics* **2004**, *43*, 2752–2759.

(12) Voloshinov, V. B.; Yushkov, K. B.; Linde, B. B. Improvement in performance of a TeO2 acousto-optic imaging spectrometer. *Journal of Optics A: Pure and Applied Optics* **2007**, *9*, 341.

(13) Hagen, N. A.; Kudenov, M. W. Review of snapshot spectral imaging technologies. *Optical Engineering* **2013**, *52*, 090901.

(14) Wagadarikar, A.; John, R.; Willett, R.; Brady, D. Single disperser design for coded aperture snapshot spectral imaging. *Applied optics* **2008**, *47*, B44–B51.

(15) Arce, G. R.; Brady, D. J.; Carin, L.; Arguello, H.; Kittle, D. S. Compressive coded aperture spectral imaging: An introduction. *IEEE Signal Processing Magazine* **2014**, *31*, 105–115.

(16) Harvey, A. R.; Fletcher-Holmes, D. W. High-throughput snapshot spectral imaging in two dimensions. Spectral Imaging: Instrumentation, Applications, and Analysis II. 2003; pp 46–55.

(17) Gao, L.; Kester, R. T.; Tkaczyk, T. S. Compact Image Slicing Spectrometer (ISS) for hyperspectral fluorescence microscopy. *Optics express* **2009**, *17*, 12293–12308.

(18) Gao, L.; Bedard, N.; Hagen, N.; Kester, R. T.; Tkaczyk, T. S. Depth-resolved image mapping spectrometer (IMS) with structured illumination. *Optics express* **2011**, *19*, 17439–17452.

(19) ElMasry, G.; Sun, D.-w. *Hyperspectral imaging for food quality analysis and control*; Elsevier, 2010; pp 3–43.

(20) Mouroulis, P.; Green, R. O.; Chrien, T. G. Design of pushbroom imaging spectrometers for optimum recovery of spectroscopic and spatial information. *Applied Optics* **2000**, *39*, 2210–2220.

(21) Kim, T. H.; Kong, H. J.; Kim, T. H.; Shin, J. S. Design and fabrication of a 900–1700 nm hyper-spectral imaging spectrometer. *Optics Communications* **2010**, *283*, 355–361.

(22) Lim, H.-T.; Murukeshan, V. M. Spatial-scanning hyperspectral imaging probe for bio-imaging applications. *Review of Scientific Instruments* **2016**, *87*, 033707.

(23) Shaw, G. A.; Burke, H. K. Spectral imaging for remote sensing. *Lincoln laboratory journal* **2003**, *14*, 3–28.

(24) Fernandez, D. C.; Bhargava, R.; Hewitt, S. M.; Levin, I. W. Infrared spectroscopic imaging for histopathologic recognition. *Nature biotechnology* **2005**, *23*, 469.

(25) Lewis, E. N.; Treado, P. J.; Reeder, R. C.; Story, G. M.; Dowrey, A. E.; Marcott, C.; Levin, I. W. Fourier transform spectroscopic imaging using an infrared focal-plane array detector. *Analytical chemistry* **1995**, *67*, 3377–3381.

(26) Hsiao, H.-H.; Chu, C. H.; Tsai, D. P. Fundamentals and applications of metasurfaces. *Small Methods* **2017**, *1*, 1600064.

(27) Kruk, S.; Kivshar, Y. Functional meta-optics and nanophotonics governed by Mie resonances. *ACS Photonics* **2017**, *4*, 2638–2649.

(28) Kamali, S. M.; Arbabi, E.; Arbabi, A.; Faraon, A. A review of dielectric optical metasurfaces for wavefront control. *Nanophotonics* **2018**, *7*, 1041–1068.

(29) Lin, D.; Fan, P.; Hasman, E.; Brongersma, M. L. Dielectric gradient metasurface optical elements. *science* **2014**, *345*, 298–302.

(30) Lalanne, P.; Astilean, S.; Chavel, P.; Cambril, E.; Launois, H. Blazed binary subwavelength gratings with efficiencies larger than those of conventional échelette gratings. *Optics letters* **1998**, *23*, 1081–1083.

(31) Wang, L.; Kruk, S.; Tang, H.; Li, T.; Kravchenko, I.; Neshev, D. N.; Kivshar, Y. S. Grayscale transparent metasurface holograms. *Optica* **2016**, *3*, 1504–1505.

(32) Zhan, A.; Colburn, S.; Trivedi, R.; Fryett, T. K.; Dodson, C. M.; Majumdar, A. Low-contrast dielectric metasurface optics. *ACS Photonics* **2016**, *3*, 209–214.

(33) Kruk, S.; Ferreira, F.; Mac Suibhne, N.; Tsekrekos, C.; Kravchenko, I.; Ellis, A.; Neshev, D.; Turitsyn, S.; Kivshar, Y. Transparent dielectric metasurfaces for spatial mode multiplexing. *Laser & Photonics Reviews* **2018**, *12*, 1800031.

(34) Arbabi, A.; Horie, Y.; Bagheri, M.; Faraon, A. Dielectric metasurfaces for complete control of phase and polarization with subwavelength spatial resolution and high transmission. *Nature nanotechnology* **2015**, *10*, 937.

(35) Liu, L.; Zhang, X.; Kenney, M.; Su, X.; Xu, N.; Ouyang, C.; Shi, Y.; Han, J.; Zhang, W.; Zhang, S. Broadband metasurfaces with simultaneous control of phase and amplitude. *Advanced Materials* **2014**, *26*, 5031–5036.

(36) Jia, S. L.; Wan, X.; Su, P.; Zhao, Y. J.; Cui, T. J. Broadband metasurface for independent control of reflected amplitude and phase. *AIP Advances* **2016**, *6*, 045024.

(37) Arbabi, A.; Arbabi, E.; Kamali, S. M.; Horie, Y.; Han, S.; Faraon, A. Miniature optical planar camera based on a wide-angle metasurface doublet corrected for monochromatic aberrations. *Nature communications* **2016**, *7*, 13682.

(38) Arbabi, A.; Arbabi, E.; Horie, Y.; Kamali, S. M.; Faraon, A. Planar metasurface retroreflector. *Nature Photonics* **2017**, *11*, 415.

(39) Afridi, A.; Canet-Ferrer, J.; Philippet, L.; Osmond, J.; Berto, P.; Quidant, R. Electrically Driven Varifocal Silicon Metalens. *ACS Photonics* **2018**, *5*, 4497–4503.

(40) Arbabi, E.; Arbabi, A.; Kamali, S. M.; Horie, Y.; Faraon, A. Controlling the sign of chromatic dispersion in diffractive optics with dielectric metasurfaces. *Optica* **2017**, *4*, 625–632.

(41) Kamali, S. M.; Arbabi, E.; Arbabi, A.; Horie, Y.; Faraji-Dana, M.; Faraon, A. Angle-multiplexed metasurfaces: Encoding independent wavefronts in a single metasurface under different illumination angles. *Physical Review X* **2017**, *7*, 041056.

(42) Zhou, Y.; Kravchenko, I. I.; Wang, H.; Nolen, J. R.; Gu, G.; Valentine, J. Multilayer Noninteracting Dielectric Metasurfaces for Multiwavelength Metaoptics. *Nano letters* **2018**, *18*, 7529–7537.

(43) Yesilkoy, F.; Arvelo, E. R.; Jahani, Y.; Liu, M.; Tittl, A.; Cevher, V.; Kivshar, Y.; Altug, H. Ultrasensitive hyperspectral imaging and biodetection enabled by dielectric metasurfaces. *Nature Photonics* **2019**, *13*, 390.

(44) Faraji-Dana, M.; Arbabi, E.; Arbabi, A.; Kamali, S. M.; Kwon, H.; Faraon, A. Compact folded metasurface spectrometer. *Nature communications* **2018**, *9*, 4196.

(45) Arbabi, A.; Arbabi, E.; Kamali, S. M.; Horie, Y.; Han, S.; Faraon, A. Increasing efficiency of high-NA metasurface lenses (Conference Presentation). High Contrast Metastructures VI. 2017; p 101130K.

Table of Content Graphics